300 mm ruling engine producing gratings and echelles under interferometric control in China

Xiaotian Li,[1,2] Haili Yu,[1] Xiangdong Qi,[1] Shulong Feng,[1] Jicheng Cui,[1] Shanwen Zhang,[1] Jirigalantu,[1] and Yuguo Tang[1,*]

[1]Grating Technology Laboratory, Changchun Institute of Optics and Fine Mechanics and Physics, Chinese Academy of Sciences, Changchun, Jilin 130033, China

[2]e-mail: lixt_1981@163.com

*Corresponding author: tangyg@sibet.ac.cn

Received 17 October 2014; revised 8 December 2014; accepted 19 January 2015; posted 22 January 2015 (Doc. ID 225177); published 27 February 2015

The designs of 300 mm ruling engine producing gratings and echelles under interferometric control (CIOMP-2) are presented. A new ruling-tool carriage system and its driving mechanism—which are easy to manufacture—are proposed. A new blank carriage system, controlled by a dual-frequency laser interferometer and a piezoelectric actuator, is designed. The CIOMP-2 ruling engine can now rule grating blanks with dimensions up to 300 mm × 300 mm, and mainly rules gratings with grating constants between 10 and 2400 lines/mm. The wavelength range of CIOMP-2 gratings is from ultraviolet to mid-infrared wavelengths. Experiments show that the new ruling-tool carriage system works well and stability of motion is improved with the help of a flexure-hinge structure, and the threefold standard deviation values of the blank carriage positioning errors are less than ~5 nm. For 600 line/mm gratings (diffraction order $m = -1$), the scatter intensities and ghosts reach 10^{-5} of the maximum intensity. The scatter intensities and ghost of gratings ruled with CIOMP-2 are low, and no Rowland ghosts are visible. The gratings ruled by CIOMP-2 have high diffraction efficiency and resolving power. CIOMP-2 can also produce varied-line-space, bend-line, and aberration-reducing gratings and echelles.

OCIS codes: (050.1950) Diffraction gratings; (050.0050) Diffraction and gratings; (120.0120) Instrumentation, measurement, and metrology; (120.4640) Optical instruments.

http://dx.doi.org/10.1364/AO.54.001819

1. Introduction

There is an urgent demand for large-area plane diffraction gratings and echelles having excellent properties in fields such as the military, aerospace, astronomy, and biochemical analysis [1–4]. The mechanical ruling method [5] has been the main method used to produce large-area infrared-laser gratings and echelles [4] that have deep grooves with strict triangular shapes.

The mechanical ruling method is the ruling of gratings using a ruling engine. Presently, the second-largest and largest ruling engines producing gratings and echelles are the MIT-B and MIT-C engines in the United States, ruling grating blanks with dimensions up to 260 mm × 430 mm and 450 mm × 635 mm, respectively [6]. The ruling-tool carriage systems and blank carriage systems of MIT-B and MIT-C are similar [6–12]. The ruling-tool carriage systems of the MIT engines [7,8] mainly comprise a cylindrical monorail, two ball bearings, a ruling-tool carriage and an optical flat. The carriage is suspended downward through ball bearings from the monorail and can swing freely, except for the restraint provided by the contact between the shoe of the carriage and the optical flat. The stability of the movement of the carriage is mainly decided by the restraint provided by the two bearings and the contact between the carriage's shoe and the optical flat

1559-128X/15/071819-08$15.00/0

[7,8]. To ensure the stable motion of the ruling-tool carriage, the precision of the mechanical production of the cylindrical monorail and the optical flat should be very high. The cylindrical monorail of MIT-C is 63 mm in diameter and 100 cm in length and its straightness in a lengthwise direction is within 274 nm [9]. The optical flat of MIT-C is 10 cm × 10 cm × 51 cm in size and its straightness in a lengthwise direction is within 69 nm [9]. The blank carriage systems of the MIT engines comprise a main carriage and a subcarriage [11,12]. The main carriage is connected to the subcarriage by specially designed flexure-hinge structures. The subcarriage can move along two metallic rolling guides. The blank carriage system of an MIT engine runs in continuous advance mode. During ruling operation, the subcarriage moves at an approximately uniform speed and the main carriage driven by a motor corrects for positioning errors of the grating blank in real time. The blank-positioning error of MIT-B is ~7 nm [8].

In this paper, a new ruling-tool carriage system and a new interferometrically controlled macro–micro stage [12]—which are easily designed, processed, and assembled—are proposed and successfully introduced into the design of the CIOMP-2 ruling engine. It has been experimentally verified that CIOMP-2 is now the world's third-largest ruling engine producing both gratings and echelles, and rules grating blanks that are up to 300 mm × 300 mm in size and have good grating performance. By interferometric control, CIOMP-2 can also produce gratings and echelles with varied line space [13], bent lines [14], and reduced aberrations [15], among others [16,17].

2. Description of CIOMP-2

CIOMP-2 was manufactured by the Changchun Institute of Optics and Fine Mechanics and Physics (CIOMP). For the past six years, CIOMP-2 has been modified to improve its grating performance in terms of the scatter intensity, ghost, and resolving power. The new structure of CIOMP-2 is shown in Fig. 1. A new ruling-tool carriage system and a new macro–micro stage have been designed, and an interferometric control method using a piezoelectric actuator and a dual-frequency laser interferometer was introduced to precisely position the blank carriage. The temperature control was also improved. The temperature can be controlled within 0.02°C. Figure 2 presents the relative position between the ruling-tool system and blank carriage system of CIOMP-2. The grating blank is mounted on the blank carriage. The blank carriage works in a stop-and-go mode. When the blank carriage is stopped, CIOMP-2 rules a grating line along the positive direction of the x axis. When the blank carriage moves (along the positive direction of the z axis), the diamond tool moves along the negative direction of the x axis and is separated from the grating blank by approximately 200–400 μm.

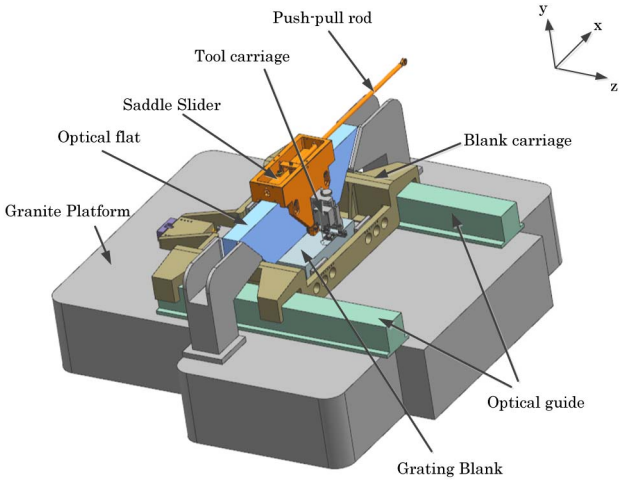

Fig. 2. Relative position between the ruling-tool system and blank carriage system.

3. Ruling-Tool Carriage System

A new ruling-tool carriage system that is easily manufactured was designed for CIOMP-2 (see Fig. 3). The system mainly comprises a saddle slider, a flexure-hinge structure (including a flexure hinge, a fixing plate, a filling piece, and a rigid shoe), a tool carriage, five rigid shoes, three spring shoes, a balance weight, and an optical flat. Our ruling-tool carriage system requires no cylindrical monorail, the construction of which would demand very high mechanical precision as in the cases of MIT-B and

Fig. 1. New structure of the CIOMP-2 engine.

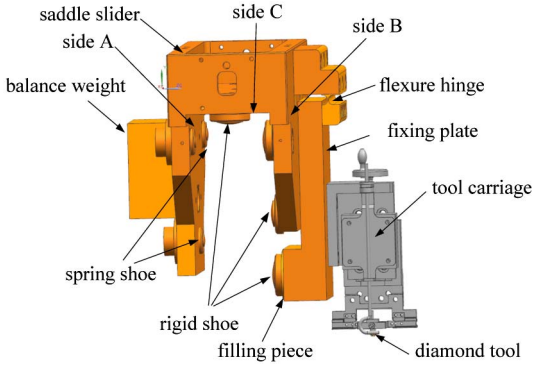

Fig. 3. New structure of the ruling-tool carriage system.

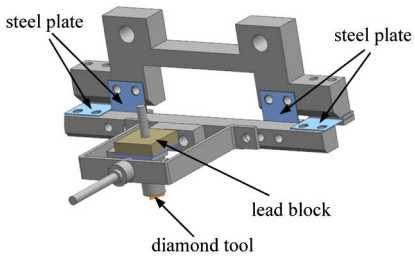

Fig. 4. Connection between the diamond tool and tool carriage.

MIT-C. Side A of the saddle slider has three spring shoes within compression springs. Side B of the saddle slider has three rigid shoes. Side C of the saddle slider has two rigid shoes. The saddle slider can move along the optical flat (see Fig. 3) with the help of the above eight shoes. The tool carriage is installed on side B of the saddle slider through the flexure-hinge structure. The balancing weight, whose function is to balance the weight of the tool carriage, is fixed on side A of the saddle slider. The thickness of the filling piece can be changed to provide a sufficient closing force between the tool carriage and optical flat. Assisted by the closure-force contact between the saddle slider and optical flat, the diamond tool moves along the optical flat and rules the grating blank as the saddle slider returns.

The diamond tool is connected to the tool carriage by two pairs of vertical and horizontal steel plates (see Fig. 4), and the weight of a lead block is used to control the grating groove depth.

Because stable movement of the ruling-tool carriage system is important to grating performance in terms of the scatter intensity and diffraction wavefront, a dual-frequency laser interferometer is adopted to measure the stability of the movement of the tool carriage (see Fig. 5). In Fig. 5, the interferometer and the optical flat are fixed on the mounting base, a long mirror is installed on the saddle slider, and the relative displacement between the long mirror and the interferometer is recorded during the movement of the saddle slider on the optical flat along the positive direction of the x axis.

Figure 6 presents four measurements of the stability of a former tool-carriage system of CIOMP-2—the main difference between the former and new ruling-tool carriage systems is that the former ruling-tool carriage system has no flexure-hinge structure and the tool carriage is directly fixed on side B of the saddle slider. Figure 7 presents four measurements of the stability of the new tool-carriage system, which has a flexure-hinge structure. In Figs. 6 and 7, the total length of movement of the tool carriage is ~66 mm. Comparing Figs. 6 and 7, it is seen that the addition of the flexure-hinge structure reduces the peak-to-valley (PV) value of the curve of the motion of the tool carriage from ~701 to ~226 nm, and reduces the nonrepeatability error of the motion of the tool carriage from ~127 to ~21 nm. The flexure-hinge structure based on the lever principle can thus greatly reduce the effect of the nonrepeatability of the movement of the saddle slider on the stability of the tool carriage. Considering the effect of the PV value of the long mirror's surface on the PV value of the curve of movement of the tool carriage, the grating-line bend error is much less than ~226 nm.

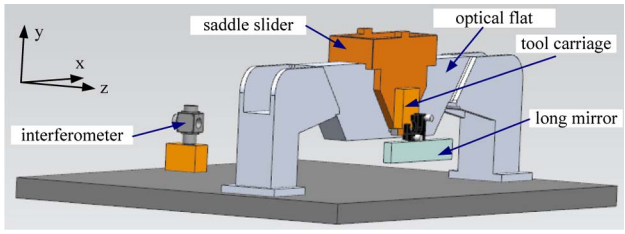

Fig. 5. Optical layout of the measurement of the stability of the tool carriage.

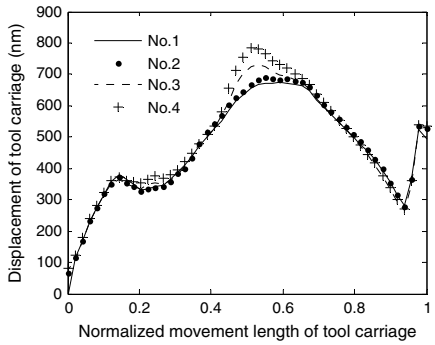

Fig. 6. Stability of a tool carriage of a former ruling-tool carriage system.

4. Driving Method of the Ruling-Tool Carriage System

In the new structure of the CIOMP-2 engine, the crank link induces a reciprocating action of the ruling-tool carriage system via the copper slide and push–pull rod (see Fig. 8). Because of the difficulty of ensuring that the two axis lines of the motions of the copper slide and ruling-tool carriage system are coincident, the connection mode among the copper slide, push–pull rod, and ruling-tool carriage system affects the grating-line bend error.

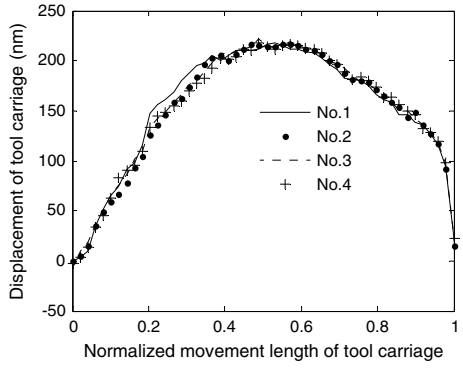

Fig. 7. Stability of the tool carriage of the new ruling-tool carriage system.

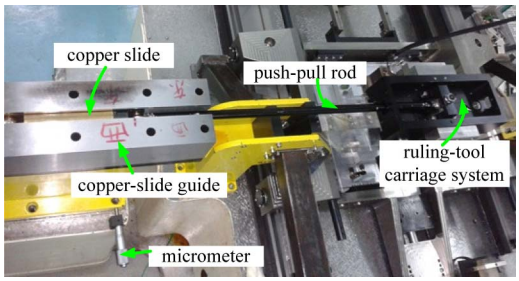

Fig. 8. Driving method of the ruling-tool carriage system.

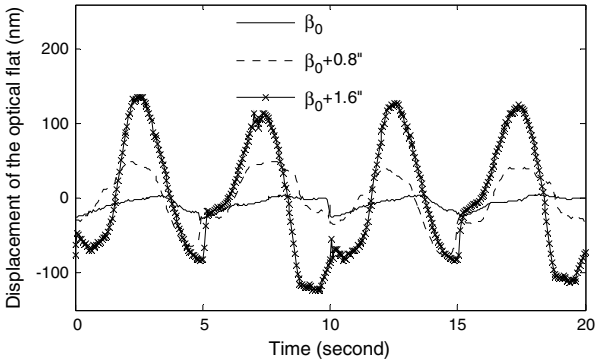

Fig. 9. Stability of the optical flat under the old drive system.

In the old mechanical structure, the connection between the copper slide and push–pull rod was flexible (e.g., a joint bearing connection) and the connection between the push–pull rod and ruling-tool carriage system was rigid (i.e., a fixed connection). This resulted in displacement of the optical flat by the laser interferometer during the reciprocating motion of the ruling-tool carriage system (see Fig. 9). In Fig. 9, three curves separately represent different displacements of the center bottom of the optical flat for different angles β between the axes of the motions of the copper slide and ruling-tool carriage system (see Fig. 10), and the reciprocating cycle of the ruling-tool carriage system is 10 s. As the angle β increases, the peak-to-valley value of the displacement of the optical flat increases. As the angle β increases from β_0 to $\beta_0 + 1.6''$, the displacement of the optical flat increases by ~109 nm.

In the new mechanical structure, both ends of the push–pull rod are connected with joint bearing structures. The displacement of the optical flat during the reciprocating motion of the ruling-tool carriage system is shown in Fig. 11. For the new connection mode of the push–pull rod, as the angle β increases, the PV

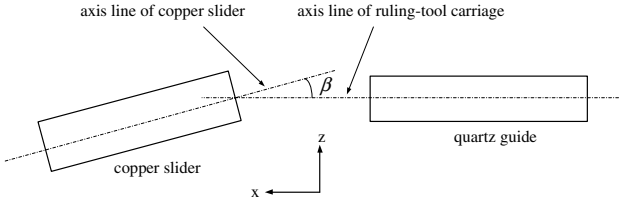

Fig. 10. Angle β between axes of the motions of the copper slider and ruling-tool carriage.

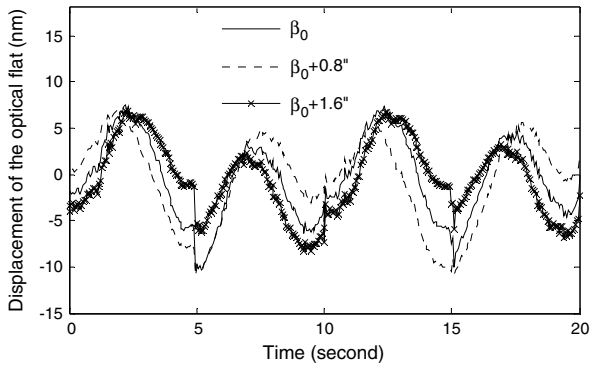

Fig. 11. Stability of the optical flat under the new drive system.

value of the displacement of the optical flat remains almost the same. The two joint bearings at the two ends of the push–pull rod greatly reduce the effect of the misalignment of the two axes of the motions of the copper slide and ruling-tool carriage system on the grating-line bend error.

5. Blank Carriage System

A new blank carriage system (see Fig. 12) based on interferometric control was designed to improve the precision of the positioning of the grating blank. The blank carriage system is a basin-type structure in appearance and mainly comprises a main carriage, a subcarriage, two optical guides, two springs, a piezoelectric actuator (PZT), and four steel plates. One side of the PZT is fixed on the subcarriage, and the other side is in frictional contact with the main carriage. The function of the two springs is to keep the piezoelectric actuator and main carriage in close contact. The main carriage is supported by four steel plates that are mounted between the main carriage and subcarriage. The subcarriage brings the main carriage along the two optical guides. A two-axis differential interferometer is introduced to measure the distance between the grating blank (see Fig. 12) and the optical flat (see Fig. 5). The measuring mirror of the interferometer is mounted on one side of the grating blank, and the referring mirror of the interferometer is mounted at the

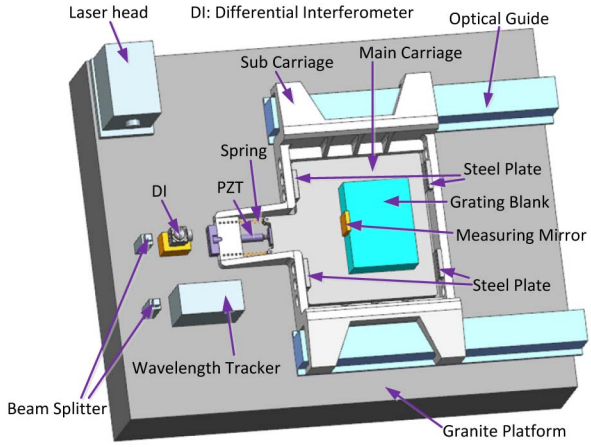

Fig. 12. Schematic of the blank carriage system.

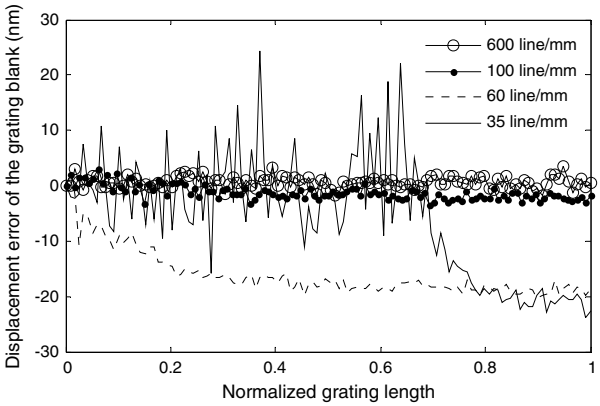

Fig. 13. Positioning error of the grating blank for different grating constants.

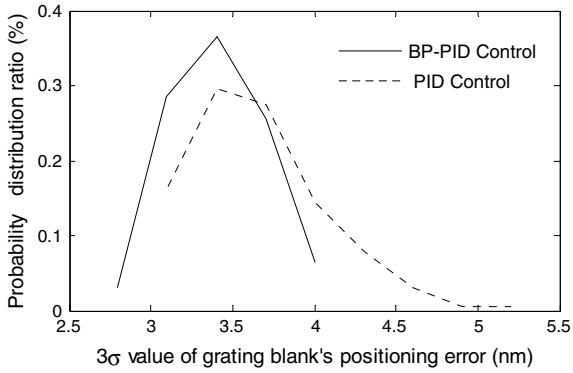

Fig. 14. Positioning error of the grating blank for the two control methods.

bottom center of the optical flat. The interferometer measures both the displacement and yaw angle of the grating blank. A wavelength tracker is adopted to compensate for the wavelength error of the interferometer.

The blank carriage system works in a stop-and-go mode. First, the subcarriage is driven by a screw–nut mechanism (see Fig. 3) to induce coarse positioning of the main carriage. The piezoelectric actuator then drives the main carriage and induces precise positioning of the main carriage with the help of the measurement made by the two-axis differential interferometer. For closed-loop control of the piezoelectric actuator, we use proportion integration differentiation (PID) control with parameters adjusted by a back-propagation (BP) neural network algorithm, BP-PID. The BP neural network structure has three layers, namely, an input layer with four nodes, a hidden layer with five nodes, and an output layer with three nodes. At the kth moment, we assume that the error signal is $E(k)$, and the proportion, integral, and differential parameters of the PID controller are $P(k)$, $I(k)$, and $D(k)$, respectively. The four nodes of the input layer are the input signal, $E(k)$, $E(k)-E(k-1)$, and $E(k)-2E(k-1)+E(k-2)$. After the training of the BP neural network algorithm, the three nodes of output layer are $P(k)$, $I(k)$, and $D(k)$. At each moment, the proportion, integral, and differential parameters of the PID controller are trained and optimized by the above BP neural network algorithm.

Figure 13 shows the positioning errors of the grating blank within one grating-line length under the conditions of the same grating-line ruling speed (6 lines/min) and closed-loop control. The figure reveals that the two grating lines having a grating constant of 35 and 60 lines/mm have large positioning errors (i.e., threefold standard deviation values of ~13 and ~33 nm, respectively). Many experiments reveal that the positioning error for a grating blank with low grating-line density (such as 35 or 60 lines/mm) mainly relates to the effect of the subcarriage motion on the positioning error of the grating blank. Under an ideal condition, the subcarriage remains still when the piezoelectric actuator is adjusting the displacement of the main carriage. Instead, when ruling a grating blank with a low grating constant, the subcarriage continues to move to a large extent because of its inertia. To solve this problem, a lower ruling speed should be chosen when ruling gratings with low grating-line density. By choosing an appropriate grating-line ruling speed to keep the ruling-tool carriage system still and using the BP-PID control method, the threefold standard deviation values of the positioning errors of the CIOMP-2 grating blank can be reduced to less than ~5 nm. Figure 14 shows the positioning errors of the grating blank when the blank carriage system moves in steps of 35 lines/mm at a grating-line ruling speed of 3 lines/min; the threefold standard deviation values of the positioning errors of the grating blank when using the BP-PID method and PID method are less than 4.1 and 5.3 nm, respectively. The BP-PID method is thus better than the PID method in controlling the CIOMP-2 blank carriage system.

6. Ruling Results

A. Commonly Used Gratings and Echelles

CIOMP in China has more than 55 years of experience in the field of grating ruling technology. The CIOMP-2 engine usually rules at a grating constant between 10 and 2400 lines/mm. Many experiments have revealed that the diffraction efficiency of the gratings ruled by CIOMP-2 can be as high as those ruled by the MIT-B and MIT-C engines. The relative diffraction efficiency—which is the ratio of the real diffraction efficiency to the theoretical diffraction efficiency—of gratings ruled by CIOMP-2 ranges approximately 85%–96%. Generally speaking, the theoretical maximum of the diffraction efficiency is proportional to the wavelength λ. As a result, the real diffraction efficiency depends on the wavelength λ also. For example, the real diffraction efficiency of a 100 line/mm grating ($\lambda = 10.6$ μm, diffraction order $m = 1$) produced with CIOMP-2 can reach ~95%, that of a 1200 line/mm grating ($\lambda = 250$ nm, $m = 1$) can reach ~70%, that of a 600 line/mm grating ($\lambda = 500$ nm, $m = 1$) can reach ~80%, and that of

Fig. 15. Diffraction light of a 600 line/mm grating ruled by CIOMP-2.

a 79 line/mm echelle ($\lambda = 632.8$ nm, $m = 36$) can reach ~60%.

Figure 15 shows the diffraction light ($\lambda = 532$ nm) for a 600 line/mm grating ruled by CIOMP-2. No Rowland ghosts were found. The scatter intensities and ghost of CIOMP-2 gratings are low in general. For 600 line/mm gratings (diffraction order $m = -1$), the scatter intensities and ghosts reach 10^{-5} of the maximum intensity.

Figure 16 shows the diffraction wavefront ($\lambda = 632.8$ nm) of order −1 for a 600 line/mm grating with a ruling area of approximately 66 mm × 70 mm ruled by CIOMP-2, where $W_{\ln}$ is the normalized length of the diffraction wavefront and W_{wn} is the normalized width of the diffraction wavefront. The PV value of the diffraction wavefront is ~0.3λ. The bend error of the grating line is small and hardly affects the PV value of diffraction wavefront. The main factor affecting the PV value of the diffraction wavefront of a CIOMP-2 grating is the displacement errors of the grating lines, which are generated by the instability of external factors such as temperature, humidity, and atmospheric pressure.

According to the diffraction wavefront of a grating, we can acquire the complex amplitude distribution of a grating's diffraction spectrum and estimate the resolution power of the grating [18]. We assume that the normalized coordinates of the diffraction wavefront are $\eta(|\eta| \le 1)$ and $\xi(|\xi| \le 1)$. Each point of the diffraction wavefront is assumed to have the same complex amplitude value. The angular coordinates of the grating's diffraction spectrum are u and v. The wavelength dispersion of the grating is along the directions of η and u. The complex amplitude of the grating's diffraction spectrum can be expressed as

$$E(u,v) = C\int_{-1}^{1}\int_{-1}^{1} e^{ik\Delta(\eta,\xi)}e^{i(u\eta+v\xi))}\mathrm{d}\eta\mathrm{d}\xi, \qquad (1)$$

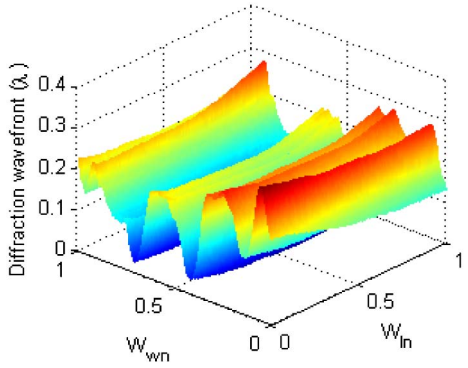

Fig. 16. Diffraction wavefront of a 600 line/mm grating.

where C is a constant and $\Delta(\eta,\xi)$ is the grating diffraction wavefront.

The normalized complex amplitude of grating's diffraction spectrum can thus be given as

$$A(u,v) = \frac{C\int_{-1}^{1}\int_{-1}^{1} e^{ik\Delta(\eta,\xi)}e^{i(u\eta+v\xi))}\mathrm{d}\eta\mathrm{d}\xi}{C\int_{-1}^{1}\int_{-1}^{1}\mathrm{d}\eta\mathrm{d}\xi} = \frac{1}{4}\int_{-1}^{1}\int_{-1}^{1} e^{ik\Delta(\eta,\xi)}e^{i(u\eta+v\xi))}\mathrm{d}\eta\mathrm{d}\xi. \qquad (2)$$

According to Eq. (2), the normalized diffraction intensity of the grating's diffraction spectrum I_G can be acquired as

$$\begin{cases} A(u,v) = \frac{f_{\mathrm{FFT}}[f_{\mathrm{FFT}}(e^{ik\Delta(m)})^T]^T}{ab} = \frac{f_{2\mathrm{FFT}}(e^{ik\Delta(m)})}{ab}, \\ I_G = A(u,v)A^*(u,v), \end{cases} \qquad (3)$$

where f_{FFT} is the fast Fourier transform function, $f_{2\mathrm{FFT}}$ is the two-dimensional fast Fourier transform function, m is the grating diffraction order, and $\Delta(m)$, having dimensions $a \times b$, is the mth-order diffraction wavefront of the grating.

Using Eq. (3), we can acquire the half width Δu of the main spectral line. Employing the Rayleigh criterion, the ratio R_r of the real resolution power to the ideal resolution power of the grating can be expressed as

$$R_r = \frac{\pi}{\Delta u} \times 100\%. \qquad (4)$$

From Eq. (3) and the diffraction wavefront shown in Fig. 16, we can obtain the two-dimensional diffraction spectrum distribution of the grating with approximate dimensions of 66 mm × 70 mm. The contours of the two-dimensional diffraction spectrum of the above CIOMP-2 grating are shown in Fig. 17, where u and v are the angular coordinates of the grating diffraction spectrum and u is the wavelength dispersion direction of the grating. The contours of the two-dimensional diffraction spectrum of the ideal grating are shown in Fig. 18. The contours in Fig. 18 are all regular with elliptical shapes. Comparing Fig. 17 with Fig. 18, we can see that the diffraction

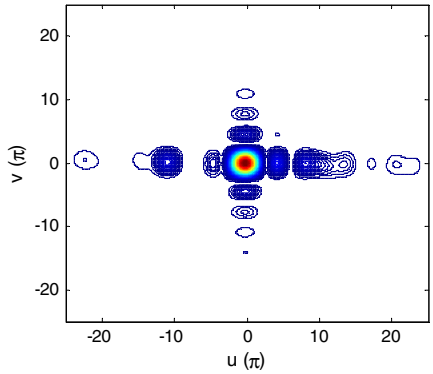

Fig. 17. Contours of the diffraction intensity of the CIOMP-2 grating.

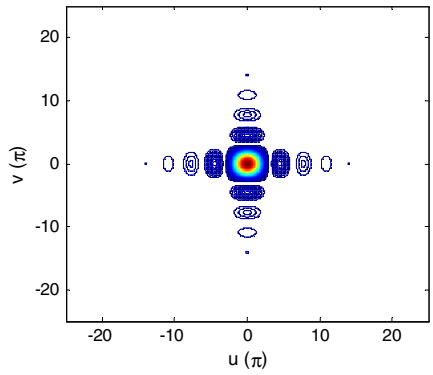

Fig. 18. Contours of the diffraction intensity of the ideal grating.

wavefront error (see Fig. 16) mainly affects the spectrum distribution along the u axis and makes the contours of the diffraction intensity become irregular. Figure 19 shows the intensity distribution of the diffraction spectrum of the above CIOMP-2 grating with approximate dimensions of ~66 mm × 70 mm when $v = 0$. From Eq. (4) and Fig. 19, we can obtain the result that the CIOMP-2 grating has very high resolution power and a resolution power ratio R_r exceeding 99%. The diffraction wavefront shown in Fig. 16 produces a few satellites near the parent line (see Figs. 17 and 18) but hardly affects the resolution power.

B. Special Gratings and Echelles

The CIOMP-2 ruling engine works in a stop-and-go mode using a piezoelectric actuator and dual-frequency laser interferometers to realize interferometric control, and it actively obtains and adjusts for grating-line displacement errors and grating-line bend errors when ruling each grating line. CIOMP-2 can thus also produce gratings and echelles with varied line space, bent lines, and reduced aberration, among others.

Figure 20 shows the diffraction wavefront of order −1 for a varied-line-spacing grating with a grating constant of 600 lines/mm and a ruling area of approximately 66 mm × 8 mm ruled by CIOMP-2, where $W_{\ln}$ is the normalized length of the diffraction

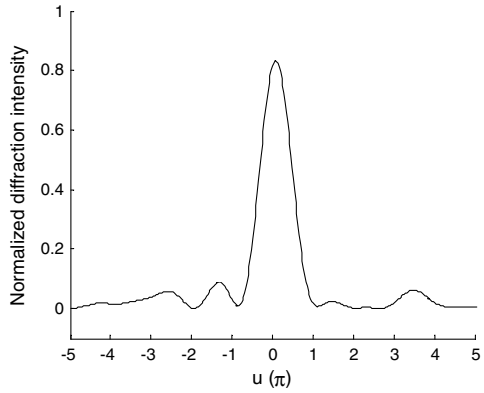

Fig. 19. Intensity distribution of the grating diffraction spectrum ($v = 0$).

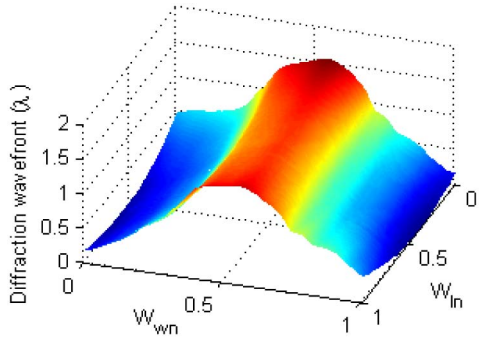

Fig. 20. Diffraction wavefront of the varied-line-space grating.

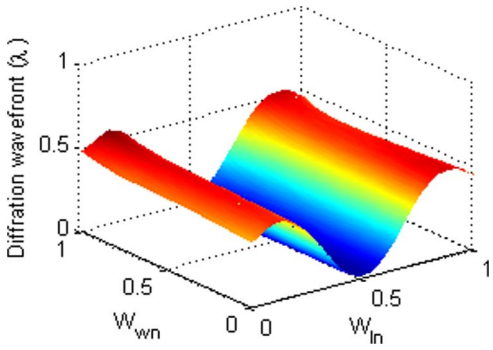

Fig. 21. Diffraction wavefront of the bend-line grating.

wavefront and W_{wn} is the normalized width of the diffraction wavefront. The shape of the varied line space is ruled to be a curved shape, and the PV value of the diffraction wavefront is 1.5λ.

Figure 21 shows the diffraction wavefront of order −1 for a bent-line grating with a grating constant of 600 line/mm and a ruling area of approximately 66 mm × 8 mm ruled by CIOMP-2. As for the varied-line-spacing grating, the shape of the bent line is ruled to be a curved shape and the PV value of the diffraction wavefront is 0.5λ.

7. Conclusions

The design and experiments on a 300 mm ruling engine with interferometric control (CIOMP-2 engine) were presented. A new ruling-tool carriage system and its driving mechanism—which are easily realized—were proposed. Experiments showed that the new ruling-tool carriage system works well and its stability of motion is improved with the help of a flexure-hinge structure. The new driving mechanism of the ruling-tool carriage system greatly reduces the effect of misalignment between the ruling-tool carriage system and its driving structure.

A new blank carriage system with interferometric control was designed. The effect of the ruling speed on grating blank positioning errors was analyzed. PID control with parameters adjusted by a BP neural network algorithm (BP-PID) was introduced to control the blank carriage.

The CIOMP-2 engine is presently the world's third-largest ruling engine producing gratings and

echelles with dimensions of 300 mm × 300 mm. CIOMP-2 mainly rules gratings with grating constants between 10 and 2400 lines/mm. The wavelength range of a CIOMP-2 grating is from ultraviolet to mid-infrared wavelengths. Using a dual-frequency laser interferometer as the measurement standard and keeping the ruling-tool carriage system still, the threefold standard deviation values of grating blank positioning errors were less than ~5 nm. Ruling experiments showed that the diffraction efficiency of the gratings ruled by CIOMP-2 can be as high as those of gratings ruled by the MIT-B and MIT-C engines. CIOMP-2 gratings have no Rowland ghosts visible. The scatter intensities and ghost of CIOMP-2 gratings are low. For 600 line/mm gratings (diffraction order $m = -1$), the scatter intensities and ghosts reach 10^{-5} of the maximum intensity. Additionally, the resolving power of a CIOMP-2 grating can reach a high level.

With the help of interferometric control, the CIOMP-2 engine can produce gratings and echelles with varied line spacing, bent lines, and reduced aberration, among others.

The authors acknowledge support from the Chinese Finance Ministry for the National R&D Projects for Key Scientific Instruments (grant ZDYZ2008-1), the Ministry of National Science and Technology for the National Key Basic Research Program of China (grant 2014CB049500), the Changchun Science and Technology Project (grant 12ZX23) in China, and the Jilin Major Province Science & Technology Development Program Project (grant 20140203011GX) in China.

Reference

1. C.-H. Chang, Y. Zhao, R. K. Heilmann, and M. L. Schattenburg, "Fabrication of 50 nm period gratings with multilevel interference lithography," Opt. Lett. **33**, 1572–1573 (2008).
2. R. Kammel, R. Ackermann, J. Thomas, J. Gotte, S. Skupin, A. Tunnermann, and S. Nolte, "Enhancing precision in fs-laser material processing by simultaneous spatial and temporal focusing," Light Sci. Appl. **3**, e169 (2014).
3. Y. T. Feng, J. Sun, Y. Li, S. N. Wang, and Q. L. Bai, "Broad-band spatial heterodyne interferometric spectrometer," Opt. Precis. Eng. **23**, 48–54 (2015), in Chinese.
4. D. Nevejans, E. Neefs, E. Van Ransbeeck, S. Berkenbosch, R. Clairquin, L. De Vos, W. Moelans, S. Glorieux, A. Baeke, O. Korablev, I. Vinogradov, Y. Kalinnikov, B. Bach, J.-P. Dubois, and E. Villard, "Compact high-resolution spaceborne echelle grating spectrometer with acousto-optical tunable filter based order sorting for the infrared domain from 2.2 to 4.3 μm," Appl. Opt. **45**, 5191–5206 (2006).
5. I. R. Bartlett and P. C. Wildy, "Diffraction grating ruling engine with piezoelectric drive," Appl. Opt. **14**, 1–3 (1975).
6. G. R. Harrison and S. W. Thompson, "Large diffraction gratings ruled on a commercial measuring machine controlled interferometrically," J. Opt. Soc. Am. **60**, 591–595 (1970).
7. G. R. Harrison, "The production of diffraction gratings I. Development of the ruling art," J. Opt. Soc. Am. **39**, 413–425 (1949).
8. G. R. Harrison and G. W. Stroke, "Interferometric control of grating ruling with continuous carriage advance," J. Opt. Soc. Am. **45**, 112–120 (1955).
9. G. R. Harrison, S. W. Thompson, H. Kazukonis, and J. R. Connell, "750-mm ruling engine producing large gratings and echelles," J. Opt. Soc. Am. **62**, 751–756 (1972).
10. G. R. Harrison, "Techniques for ruling improved large diffraction gratings," Final Report N71-17173 (Massachusetts Institute of Technology, 1971), pp. 1–14.
11. G. R. Harrison and N. Sturgis, "Interferometrically controlled ruling of ten-inch diffraction gratings," J. Opt. Soc. Am. **49**, 205–211 (1959).
12. G. R. Harrison and N. Sturgis, "Ruling of large diffraction gratings with interferometric control," J. Opt. Soc. Am. **47**, 15–22 (1957).
13. Q. Ling, G. Wu, B. Liu, and Q. Wang, "Varied line spacing plane holographic grating recorded by using uniform line spacing plane gratings," Appl. Opt. **45**, 5059–5063 (2006).
14. B. Liu, Q. Wang, S. Fu, and Z. Hu, "Generalized groove density equation concerning bending-grating-related imaging properties," J. Opt. Soc. Am. A **23**, 1135–1140 (2006).
15. T. Harada and T. Kita, "Mechanically ruled aberration-corrected concave gratings," Appl. Opt. **19**, 3987–3993 (1980).
16. H. L. Yu, X. T. Li, J. W. Zhu, H. Z. Yu, X. D. Qi, and S. L. Feng, "Reducing the line curvature error of mechanically ruled gratings by interferometric control," Appl. Phys. B **117**, 279–286 (2014).
17. X. T. Li, X. D. Qi, H. L. Yu, J. X. Gao, S. L. Feng, and Bayanheshig, "Yaw angle correction of grating line based on single piezoelectric actuator," Opt. Precis. Eng. **22**, 2039–2046 (2014), in Chinese.
18. G. W. Stroke, *Handbuch der Physik*, S. Flugge, ed. (Springer, 1967) **29**, p. 445–574.